



HAL
open science

Wavelet-based 3D reconstruction of microcalcification clusters from two mammographic views: new evidence that fractal tumors are malignant and Euclidean tumors are benign

K. A. Batchelder, A. B. Tanenbaum, S. Albert, L. Guimond, P. Kestener, A. Arneodo, A. Khalil

► To cite this version:

K. A. Batchelder, A. B. Tanenbaum, S. Albert, L. Guimond, P. Kestener, et al.. Wavelet-based 3D reconstruction of microcalcification clusters from two mammographic views: new evidence that fractal tumors are malignant and Euclidean tumors are benign. PLoS ONE, 2014, 9 (9), pp.e107580. 10.1371/journal.pone.0107580 . hal-01557073

HAL Id: hal-01557073

<https://hal.science/hal-01557073>

Submitted on 23 Sep 2022

HAL is a multi-disciplinary open access archive for the deposit and dissemination of scientific research documents, whether they are published or not. The documents may come from teaching and research institutions in France or abroad, or from public or private research centers.

L'archive ouverte pluridisciplinaire **HAL**, est destinée au dépôt et à la diffusion de documents scientifiques de niveau recherche, publiés ou non, émanant des établissements d'enseignement et de recherche français ou étrangers, des laboratoires publics ou privés.



Distributed under a Creative Commons Attribution 4.0 International License



Wavelet-Based 3D Reconstruction of Microcalcification Clusters from Two Mammographic Views: New Evidence That Fractal Tumors Are Malignant and Euclidean Tumors Are Benign

Kendra A. Batchelder^{1,2,3}, Aaron B. Tanenbaum^{1,2,3}, Seth Albert^{1,2,3}, Lyne Guimond^{1,2,3}, Pierre Kestener⁴, Alain Arneodo^{5,6}, Andre Khalil^{1,2,3*}

1 CompuMAINE Lab, University of Maine, Orono, Maine, United States of America, **2** Department of Mathematics and Statistics, University of Maine, Orono, Maine, United States of America, **3** Institute for Molecular Biophysics, University of Maine, Orono, Maine, United States of America, **4** Commissariat à l'Energie Atomique, Gif-sur-Yvette, France, **5** Laboratoire de Physique, Ecole Normale Supérieure de Lyon, Lyon, France, **6** Centre National de Recherche Scientifique, Ecole Normale Supérieure de Lyon, Lyon, France

Abstract

The 2D Wavelet-Transform Modulus Maxima (WTMM) method was used to detect microcalcifications (MC) in human breast tissue seen in mammograms and to characterize the fractal geometry of benign and malignant MC clusters. This was done in the context of a preliminary analysis of a small dataset, via a novel way to partition the wavelet-transform space-scale skeleton. For the first time, the estimated 3D fractal structure of a breast lesion was inferred by pairing the information from two separate 2D projected mammographic views of the same breast, i.e. the cranial-caudal (CC) and mediolateral-oblique (MLO) views. As a novelty, we define the “CC-MLO fractal dimension plot”, where a “fractal zone” and “Euclidean zones” (non-fractal) are defined. 118 images (59 cases, 25 malignant and 34 benign) obtained from a digital databank of mammograms with known radiologist diagnostics were analyzed to determine which cases would be plotted in the fractal zone and which cases would fall in the Euclidean zones. 92% of malignant breast lesions studied (23 out of 25 cases) were in the fractal zone while 88% of the benign lesions were in the Euclidean zones (30 out of 34 cases). Furthermore, a Bayesian statistical analysis shows that, with 95% credibility, the probability that fractal breast lesions are malignant is between 74% and 98%. Alternatively, with 95% credibility, the probability that Euclidean breast lesions are benign is between 76% and 96%. These results support the notion that the fractal structure of malignant tumors is more likely to be associated with an invasive behavior into the surrounding tissue compared to the less invasive, Euclidean structure of benign tumors. Finally, based on indirect 3D reconstructions from the 2D views, we conjecture that all breast tumors considered in this study, benign and malignant, fractal or Euclidean, restrict their growth to 2-dimensional manifolds within the breast tissue.

Citation: Batchelder KA, Tanenbaum AB, Albert S, Guimond L, Kestener P, et al. (2014) Wavelet-Based 3D Reconstruction of Microcalcification Clusters from Two Mammographic Views: New Evidence That Fractal Tumors Are Malignant and Euclidean Tumors Are Benign. PLoS ONE 9(9): e107580. doi:10.1371/journal.pone.0107580

Editor: Chin-Tu Chen, The University of Chicago, United States of America

Received: January 21, 2014; **Accepted:** August 20, 2014; **Published:** September 15, 2014

Copyright: © 2014 Batchelder et al. This is an open-access article distributed under the terms of the Creative Commons Attribution License, which permits unrestricted use, distribution, and reproduction in any medium, provided the original author and source are credited.

Funding: This work was funded through a grant from the Maine Cancer Foundation, as well as funds from the Institute for Molecular Biophysics and the Department of Mathematics at the University of Maine. The funders had no role in study design, data collection and analysis, decision to publish, or preparation of the manuscript.

Competing Interests: The authors declare the patent application: PCT/US14/35153; Title: IMPROVED METHODS OF CANCER DETECTION; Applicant: University of Maine System Board of Trustees; Filed: April 23, 2014 Inventors: Andre Khalil & Kendra Batchelder. This does not alter the authors' adherence to all PLOS ONE policies on sharing data and materials.

* Email: andre.khalil@maine.edu

Introduction

Breast cancer is the most common cancer worldwide according to the World Health Organization (WHO) and the second leading cause of cancer related death among women in the United States. Despite the recent advances in the medical field, the breast cancer rate has continued to increase over the last 30 years. Cancer is easiest to treat when it is found in the early stages of development, making it critical for women to have regular screenings as recommended by the American Cancer Society (ACS). Mammograms are currently one of the most accepted screening processes and are widely recognized to play a vital role in diagnosing the disease. However, the radiological interpretation of mammograms

is a difficult task, especially since the mammographic appearance of normal tissue is highly variable. Even though mammograms are typically read by two expert radiologists or a combination of a radiologist with a computer aided detection/diagnosis (CAD) method, a recent study suggests that a minimum of three independent experts combined with a consensus should be used, especially for non-cancer cases [1]. Criticism of the use of screening mammography due to over-diagnosis led some researchers to show that one in three breast cancers identified by mammography would not cause symptoms in a patient's lifetime [2]. Others argue that advanced breast cancer incidence does not support a substantial role for screening in the decrease in mortality [3]. The recent decline in breast cancer mortality would not be

due to population-based screening programs, but rather to improved treatments of the sick [4,5].

This growing wave of criticism of breast cancer screening programs has been synchronous to a similar movement criticizing the increasing use of CAD methods. We hypothesize that this is *not* a coincidence. Indeed, it has been fifteen years since the U.S. Food and Drug Administration approved usage of CAD methods. From 2001 to 2006, CAD prevalence increased from 3.6% to 60.5% and has since increased to about 75% [6]. However, CAD methods are not offering the expected performance [7]. CAD use in screening mammography is associated with decreased specificity [8]. This leads to increased recall rates of healthy women [6,9,10] and can cause false-positives on up to 70% of normal cases [11], resulting in an increase of unnecessary stress on women. In a study that compared the effectiveness of a single reader + CAD vs. two independent readers, the results showed that the recall rate for single reader + CAD was higher [12]. And finally, another limitation of existing CAD methods is the inability of the software to rate the significance of the findings [13], similar to the Breast Imaging-Reporting and Data-System (BI-RADS) assessment score [14] given by the radiologist at the time of the mammogram interpretation.

Despite these potentially worrisome signals, the consensus is that the benefits of screening mammography clearly outweigh the disadvantages. In fact, the use of screening mammography is not expected to diminish, but rather to increase. The American Cancer Society (ACS) recommendation is for women age 40+ to have a mammogram every year and to continue to do so for as long as they are in good health. In England, for example, the extension of the breast screening program, from women aged 50–70 to 47–73 is expected to be completed in 2016 [15]. Taken together, this information combined with the results surveyed above indicates that novel computational techniques must be developed, not only to obtain better quantitative mammography reports, but also to better understand the onset and progression of the disease itself.

The fractal dimension is a tool that has been used extensively in all sciences. While standard geometry is limited to the study of so-called Euclidean objects like smooth curves, circles, and cubes, Fractal geometry can be seen as a generalization of Euclidean geometry, where the study of objects exhibiting a geometrical structure that cannot be described with Euclidean tools such as area, perimeter, and volume, becomes naturally characterized, quantitatively, via the fractal dimension. Standard Euclidean geometrical objects have an integer fractal dimension ($D = 1, 2, 3$ for a line, circle and cube respectively), while most (tree-like or filamentary) fractal objects have a non-integer fractal dimension [16].

The link between the fractal nature of malignant growth and pathology in general has been well established [17–20]. For example, specific applications of fractal concepts were used to quantitatively characterize skin lesions [21–23], the tumor vasculature and the tissue architecture at the cellular level [24–26], as well as the epithelia/stroma interface [27,28]. The application of fractal concepts specifically to the analysis of breast cancer from the study of digitized mammograms is widespread. For example, fractal-based models of (normal) breast tissue background are used to find calcifications by taking the difference between the original mammographic image and the modeled image [29–31]. To assess the actual fractal structure of the periphery of the tumor itself, some use the radiologist-identified boundary of masses using different techniques to show that this manually drawn contour is more likely to be smooth (Euclidean) for benign tumors and more spiculated (fractal) for malignant

tumors [32–34]. In an early study of 25 mammographic cases (10 benign and 15 malignant) investigating the potential utility of the fractal dimension of clusters of microcalcifications as a discriminatory quantifier, 14 out of 15 malignant cases were able to be separated using the fractal dimension [35]. Another study using fractal models with neural networks to detect microcalcifications attempted to quantitatively characterize the clustering of the segmented calcification spots via the fractal dimension. However, the fractal dimension was insufficient to discriminate between actual microcalcification clusters from sets of noise spots, when considering one mammographic view at a time [36].

Since clusters of microcalcifications are one of the most important and often the only indicator for malignant tumors, the reconstruction of the three-dimensional (3D) structure of these clusters from the two mammographic views, cranial-caudal (CC) and mediolateral-oblique (MLO), is critically important. An early attempt at developing a 3D visualization software putting additional diagnostic information at the radiologists disposal was presented fifteen years ago [37]. More recently a joint analysis of two views of the same breast was presented, where the novelty of the scheme includes a two-step matching process: spatial and feature matching. The authors show that the proposed method has advantages of a lower false positive rate compared to the one on a single view [38]. Taken together, this shows that very little has been done in order to quantitatively combine the information obtained from both views, even though it appears to be logical and beneficial from the research. Overall, however, a reliable quantitative assessment methodology in the form of a computer-aided diagnostic system integrating the fractal structure from both mammographic views is lacking. This is what we are proposing in this manuscript, with very promising results.

We propose that the 2D Wavelet Transform Modulus Maxima (WTMM) method [39] has the ability to become a powerful tool in interpreting mammograms. The 2D WTMM method has proven to be successful in almost all fields of applied science, including geology [40], astrophysics [41–43], surface science [44], cellular biology [45–51] and orthopedic medicine [52]. The method was originally developed as a multifractal formalism to analyze highly complex 1D signals [53,54], 2D surfaces [40,55,56] and 3D surfaces [57]. In particular, the 1D WTMM method was successfully applied to demonstrate the multifractality in physiologic dynamics and its breakdown with disease [58–62]. A preliminary approach demonstrating the potential of the 2D WTMM method to detect microcalcifications and to quantitatively assess and discriminate between fatty vs. dense tissue was first presented in 2001 [63].

The results presented in this paper were obtained by using the WTMM method on screening mammograms that were taken from an online databank. They demonstrate how this tool could be used as a possible Computer-Aided *Detection* method as well as a Computer-Aided *Diagnostic* method. After all images were analyzed using this method, the fractal information independently obtained from each of the two mammographic views of the same breast was combined to indirectly infer a 3D estimate of the geometrical structure of the breast tumor. A statistical analysis was performed on all data, which provided us with information on the critical differences between the organization of both benign and malignant tumors. Importantly, both views of the same breast (CC and MLO) were analyzed independently in terms of microcalcification detection and fractal dimension estimation. The differences in fractal dimension between benign vs. malignant MC clusters were very significant when using population-based statistics. However, in order to develop a diagnostic scheme that would provide high accuracy categorization on a case-by-case

basis, the fractal dimension of the cluster of microcalcifications from both views was integrated into a two-coordinate score that was used to plot each case in the “CC-MLO fractal dimension plot”. In this plot we have defined a “fractal zone” consisting almost exclusively of malignant cases and “Euclidean zones” (non-fractal) consisting almost exclusively of benign cases. Therefore, as a potential diagnostic tool, this methodology could be used to assist radiologists by calculating an assessment based on a particular case’s position in the CC-MLO fractal dimension plot, and whether or not it is inside or outside the fractal zone. It can do this with high accuracy and in a manner that is independent of the density of the background tissue. Furthermore, the fractal vs. Euclidean distinction between malignant vs. benign tumors, could lead to a better understanding of the biophysical processes that drive tumor growth.

Results

Detection of MC Clusters and Calculation of their Fractal Dimension

As described in detail in the Methods section and in Figure 1, the wavelet transform (WT) acts as a mathematical microscope to characterize spatial image information over a continuous range of size scales. It is the gradient vector of the image smoothed by dilated versions of a Gaussian filter [39,64]. At each size scale, the wavelet transform modulus maxima (WTMM) are defined by the positions where the modulus of the WT is locally maximal. These WTMM are automatically organized as maxima chains at the considered scale. Along each of these chains, further local maxima are found, i.e., the WTMM maxima (WTMMM). This process is repeated for all size scales and the WTMMM from each scale are then linked to form the WT skeleton. As shown in Figures 2 and 3, the ability to consider (vertical) space-scale WTMMM lines in the WT skeleton individually is key, since it allows us to objectively discriminate between lines pointing to the tissue background from those pointing to the microcalcifications by considering how the WT modulus varies as a function of the scale parameter along each space-scale line. In Figures 2D and 3D, each space-scale line obtained from the WT skeleton is represented by plotting the evolution of the WT modulus, M (see Eq. (6) in the Methods section), as a function of the scale parameter, a , in a log-log plot. This relationship between M and a is characterized by a power-law behavior via the equation:

$$M = K a^h \quad (1)$$

where K is a pre-factor and h is the Hölder exponent quantifying the strength of the singularity to which the space-scale line is pointing to. In log-log plots shown in Figures 2D and 3D, the slope of the curves therefore corresponds to h . By considering two types of information characterizing the behavior of a space-scale line, namely the strength of the modulus at the smallest scale, which is given by the log of the pre-factor, $\log(K)$, as well as the slope (in a logarithmic representation) of the modulus variation across scales, h , a classification procedure is setup which results in two sets of space-scale lines that clearly segregate MC from background tissue. Isolated MC can be seen as Dirac-like singularities through the optics of the WT, for which h is theoretically known to be -1 [39]. However, while clustered MC may not appear as isolated Dirac-like singularities, the edge that they form is still easily detectable through the space-scale lines, with a value of $h \sim 0$ (discontinuity). This means that for both isolated and clustered MC, we can expect the space-scale lines to behave as Eq (1) with $h \leq 0$, which contrasts from the healthy background tissue, for

which $h \sim 1/3$ for fatty breast tissue and $h \sim 2/3$ for dense breast tissue [63]. However, relying only on h may not be sufficient, which is why the strength of the WT modulus at the lowest scale, which quantifies the contrast between MC and background, is also needed. For the sample case presented in Fig. 2, the plot in Fig. 2D shows that neither $\log(K)$ nor h , taken individually, would have been sufficient to segregate between MC and background. However, for the sample case presented in Fig. 3, the plot in Fig. 3D shows that $\log(K)$ alone was sufficient. A more detailed discussion of both cases follows.

In Fig. 2 the background breast tissue is dense, which makes the contrast between background and MC weak (i.e. causing a low value for the WT modulus of red curves at the smallest scale in Fig. 2D). However, the roughness fluctuations of dense breast tissue are characterized by a relatively high smoothness level, which translates to blue curves with a large slope (i.e., a high h value, $\sim 2/3$) for scales $10 \leq a \leq 200$ pixels as compared to the red curves with negative slopes for scales $a \geq 10$ pixels that correspond to WTMMM lines that point to MC at small scale ($a \rightarrow 0^+$) (Fig. 2D) [63]. In Fig. 3, the background breast tissue is fatty, which is characterized by a higher roughness level (i.e. a lower h value $\sim 1/3$, although still positive) [63], that reduces the discriminatory power of h . However, for MC embedded into fatty tissue, the contrast is high, which translates to a high value of $\log(K)$. Therefore, applying a threshold on both parameters, h and $\log(K)$, is key to segregating MC from their background regardless of the density (fatty or dense) of the composition of the breast tissue. Given the exploratory nature of this study, the thresholds on h and $\log(K)$ were allowed to vary from one image to another and they were set manually. However, the variability of these thresholds is rather small (data not shown), which shows great potential for a future automation of this processing step.

Once this segregation is done, the so-called singularity spectrum (see Methods section) can then be calculated separately for each subset, which then allows us to consider the fractal dimension D (Eq. (16)) of the lesion, characterizing its architecture.

We restricted the analysis of DDSM cases (see Methods section) to images having a radiologist encircled region that was larger than 256^2 pixels for both views (CC and MLO) and also to make sure that the distribution of patient ages was comparable (i.e. 56.7 ± 11.4 years old for the benign cases and 65.5 ± 12.4 years old for the malignant cases). This resulted in an analyzed sample with a total of 59 cases (118 images), 34 of which are benign (68 images) and 25 of which are malignant (50 images). The histograms of fractal dimension values obtained are presented in Figure 4. Note that blending the CC and MLO fractal dimensions together in these distributions would not guarantee an unbiased statistical analysis, which is why the fractal dimension values for the CC and MLO results were analyzed independently. Figure 4 demonstrates that benign MC clusters have a strong preference for Euclidean dimensions that are either close to $D = 1$ or to $D = 2$ and that there is a very clear zone of avoidance in the fractal range, i.e., for $1 < D < 2$, with an actual gap in the benign histograms for the bin centered at $D = 1.5$ for both views. For the malignant cases, it is the opposite: Euclidean zones are avoided and the data are very clearly centered in the fractal range for both views, with the peak of the histograms at $D = 1.5$. A statistical comparison between benign vs. malignant MC clusters was performed using the Wilcoxon rank-sum test, which yielded p -values of 0.009 for CC comparisons and 0.014 for MLO comparisons for the benign vs. malignant fractal dimension distributions. These are statistically significant differences.

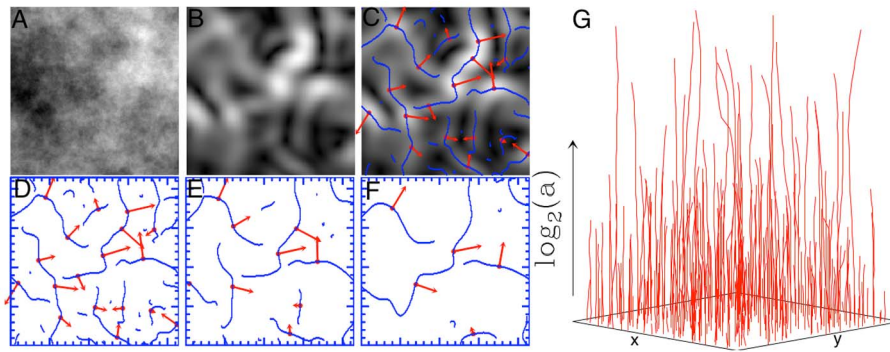


Figure 1. The 2D WTMM Method. (A) Sample simulated fractional Brownian motion image $B_{H=0.5}(\mathbf{x})$ [39]. (B) The gradient of the image in (A) is obtained as the modulus of the wavelet-transformed using Eq. (6). (C) Maxima chains in blue are defined as positions where the WT modulus is locally maximal (i.e., the WTMM). Along these WTMM chains in (C), further local maxima are found in red, i.e. the WTMMM. This is repeated at several different scales, three of which are shown in (D), (E), and (F). The WTMMM are then connected vertically through scales to define the WT skeleton shown in (G). Gray-scale coding is from black (min) to white (max).
doi:10.1371/journal.pone.0107580.g001

The CC-MLO Fractal Dimension Plot and the Fractal Zone

The significance of the difference between benign and malignant is quite interesting. However, it is still only based on statistics of populations. The histograms in Figure 4 show that, when each view is taken independently (CC or MLO), it is still possible, though unlikely, for a malignant lesion to have a Euclidean dimension, and vice-versa, for benign lesions to have a (non-integer) fractal dimension. However, in order to work towards a potential CAD method that would be able to diagnose breast lesions individually instead of via the population statistics, we combined the information to indirectly infer the 3D structure of the tumor embedded into the breast tissue. This is presented in a novel plot called the “CC-MLO fractal dimension plot” shown in Figure 5, where red dots represent malignant cases and green dots represent benign cases. The square centered at (1.5, 1.5) represents those cases for which both CC and MLO views have a

fractal dimension that is within $1.2 < D < 1.8$. Note that only malignant cases are found in this internal square. However, having one of the two views with a score that is close to $D = 1.5$ should “compensate” for its other view being outside of the $[1.2, 1.8] \times [1.2, 1.8]$ square, i.e., as one view approaches $D = 1.5$, the farther from 1.5 the other can be. Further justification is presented below and in Fig. 6. That is how the triangular regions that decay linearly as a function of distance from the internal square were defined. Therefore, the central square, combined with the four triangular regions extending from it are what we define as the “fractal zone”. Of the 59 cases considered in this study, 92% of malignant breast lesions studied (23 out of 25) were in the fractal zone while 88% of the benign lesions were in the Euclidean zones (30 out of 34).

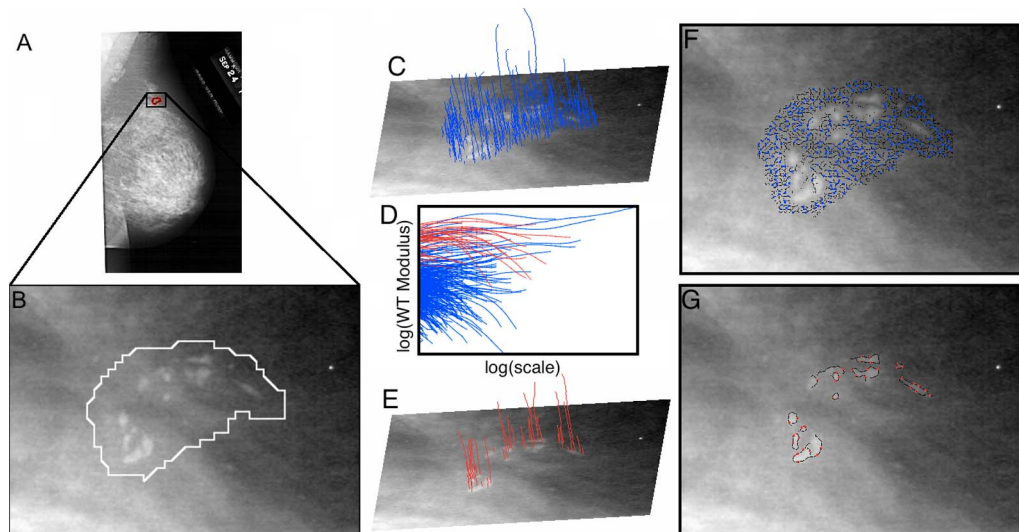


Figure 2. Sample 2D WTMM analysis of a malignant breast lesion. (A) Original image obtained from the DDSM database, where (B) shows the zoomed in image of the radiologist circled suspicious region. By selecting appropriate values for the slope h of the WT modulus as a function of scale in a logarithmic representation, and the log of the pre-factor, $\log(K)$ in (D) (also see Eq. (1) in the main text that describes this relationship), the WTMMM (blue) from the tissue background in (C) are distinguished from the WTMMM (red) that belong to the MC in (E). From here the WT skeleton can be calculated from the WTMMM that belong to the lesion from those that belong to the background tissue. The corresponding WTMM chains at the smallest scale are shown in (F) and (G) for the background and lesion, respectively.
doi:10.1371/journal.pone.0107580.g002

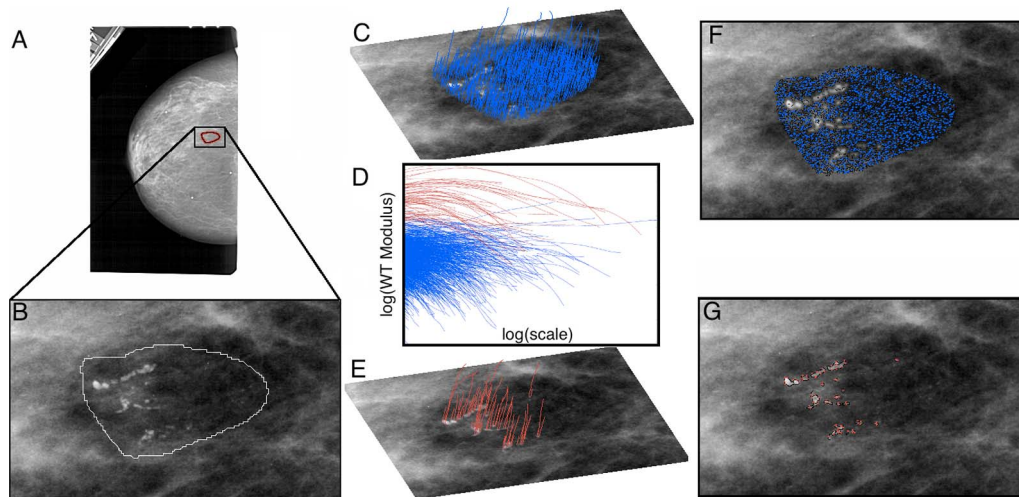


Figure 3. Sample 2D WTMM analysis of a second malignant breast lesion. Same analysis as presented in Figure 2, but on a different case. doi:10.1371/journal.pone.0107580.g003

Bayesian analysis

The inferences from a Bayesian analysis are richer and more informative than null hypothesis significance testing. In particular, there is no reliance on p -values. But also, Bayesian models are designed to be appropriate to the data structure without having to make approximation assumptions typical in null hypothesis significance testing [65]. The results reported above obviously show that the vast majority of malignant breast lesions are fractal, and that the vast majority of benign breast lesions are Euclidean. However, the condition of interest is how breast lesions in the fractal zone can indicate malignancy, and how breast lesions in the Euclidean zone can indicate benignancy.

Bayesian inference derives the posterior probability as a consequence of two antecedents, a prior probability and a likelihood function derived from a probability model for the data

to be observed. In this application, the model is based on historical radiology assessment scores using the BI-RADS system [14,66,67]. A detailed description of this probability model as well as the mathematical model behind Bayes analysis is presented in the Methods section. Bayesian inference then becomes a computation of the posterior probability according to Bayes' rule. The interpretable output of this Bayesian analysis is the so-called 95% highest density interval (HDI), which is analogous to the 95% confidence interval in frequentist statistics. The 95% HDI from the resulting posterior distribution indicates that the percentage of breast lesions in the fractal zone that are malignant is between 74.2% and 97.5%. Alternatively, in terms of controlling for false positives, which is a major concern, as discussed in the Introduction, the percentage of breast lesions in the Euclidean zone that are benign is between 75.7% and 96.2%.

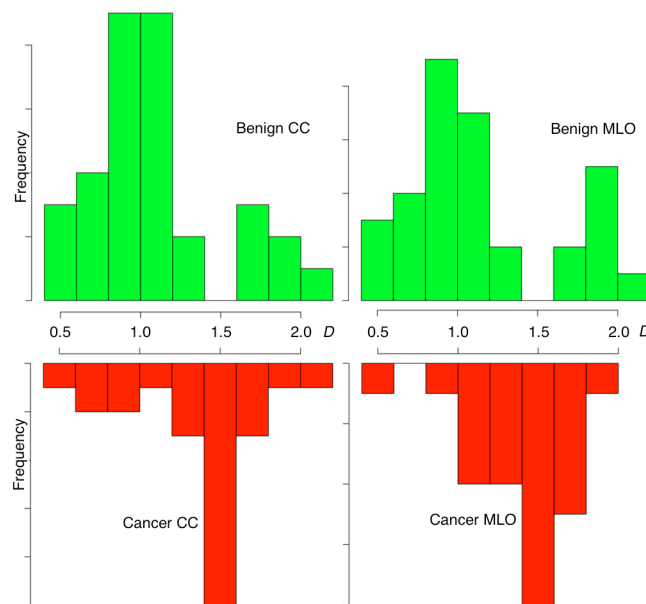


Figure 4. Histograms of fractal dimension values. The frequency distributions of fractal dimensions, D (Eq. (16)) calculated for benign CC and MLO views (top) are drastically different than those calculated for the cancer CC and MLO views (bottom). doi:10.1371/journal.pone.0107580.g004

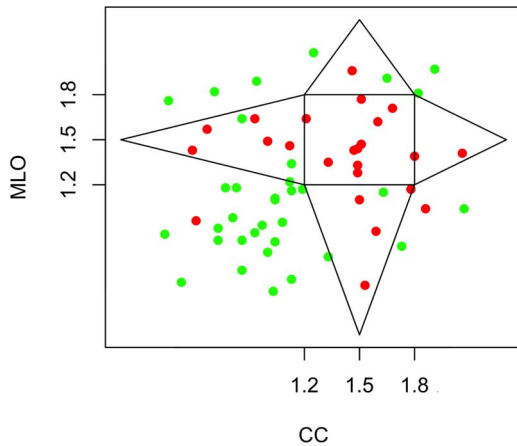


Figure 5. The CC-MLO fractal dimension plot. Each case analyzed is plotted with the fractal dimension obtained from the MLO view as a function of the fractal dimension obtained from the CC view. A polygonal region is outlined, the inside of which is defined as the “fractal zone” while the outside is defined as the “Euclidean zone”. The dots represent malignant (red) and benign (green) cases. doi:10.1371/journal.pone.0107580.g005

Additional statistical analysis

The Bayesian analysis presented above takes into account the limited size of the dataset and the robust statistical conclusions that are drawn from this analysis are indeed significant. Nevertheless, an additional statistical analysis was performed in order to further validate the significance of our results. Instead of constructing a statistical estimator and evaluating its frequency properties, a statistical model was developed by constructing a joint probability distribution and by checking it against the observational data, as suggested in [68]. A “coin toss” experiment was performed 100,000 times (see Methods section) to arrive at a discrete probability distribution, which showed that the model was an adequate representation of the data, as demonstrated by the red bars being at neither end of the distributions in Figures 7A and 7B. Indeed, the probability that the number of malignant cases (out of the 27 fractal cases) is less than 23, is $\sim 46\%$. Alternatively, the probability that the number of benign cases (out of the 32 Euclidean cases) is less than 30, is $\sim 74\%$. Both percentages (46%

and 74%) being close to 50% is further validation that our results are not outliers in the model (e.g. $<5\%$ or $>95\%$). Therefore, we can safely say that the model is an adequate fit for the data.

Interpretation of the 3D Geometrical Structure

Even though two different 2D views of a 3D object are insufficient to fully characterize its 3D geometry, it can nonetheless give a robust estimate. The cases outside of the fractal zone can be categorized in two Euclidean subsets: 1) LINES, i.e. those that are approximately in the $(D_{CC}=1, D_{MLO}=1)$ area, which are therefore seen as one-dimensional objects from both views (Fig. 6A); or 2) SHEETS, i.e. those that are either in the $(D_{CC}=1, D_{MLO}=2)$ or $(D_{CC}=2, D_{MLO}=1)$ areas, which are seen as a full two-dimensional object in one view, but as a one-dimensional object from the other view and also those that are in the $(D_{CC}=2, D_{MLO}=2)$ area, which are seen as a full two-dimensional object from both views (Fig. 6B). Although simplistic, these case models represent a good estimate of what the 3D Euclidean structure of a benign lesion may look-like.

For the cases that fall in the fractal zone, those malignant lesions that are in the $[1.2,1.8] \times [1.2,1.8]$ square have a fractal signature that is seen from both views, whereas those that are in the triangular areas would represent fractal clusters that grow onto a 2D plane, i.e. seen as a fractal from one view, but seen either as a line (bottom or left triangular regions) or a plane (top or right triangular regions) from the other view (Fig. 6C). Interestingly, a diffusion-limited aggregate [69] embedded in 3D space and for which $2 < D < 3$ will have a 2D projection with $D = 2$ [70]. Since no malignant lesions are found in the $(D_{CC}=2, D_{MLO}=2)$ area of the CC-MLO fractal dimension plot, we can safely hypothesize that all tumors are essentially limited to a 2-dimensional fractal structure (within the 3-dimensional breast tissue), for which $1 < D < 2$ [71,72]. This therefore leads us to conjecture that all breast tumors considered in this study, benign and malignant, fractal or Euclidean, would grow on 2-dimensional manifolds.

Conclusion & Discussion

Early detection and characterization of breast lesions are critical for the treatment and survival of the patient. Thus, the methodology presented here offers a way to accurately classify benign and malignant tumors based on their invasiveness determined by the geometrical structure obtained using this

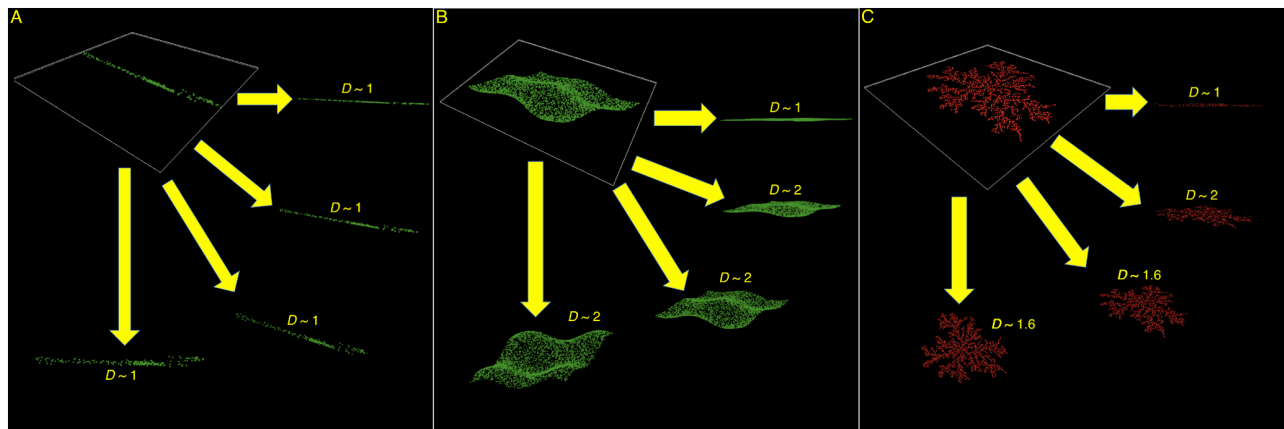


Figure 6. Inferring the 3D geometrical structure of breast lesions based on projection angles. Simulations of random point distribution models are shown to describe how different types of objects, namely a line (A), a surface (B), and a fractal cluster (simulated diffusion-limited aggregate, C) can have only a limited number of possible fractal dimension as a function of the projection angle. doi:10.1371/journal.pone.0107580.g006

methodology. By considering the organization of tumors via CAD systems, current mammographic practice may be improved by increasing accuracy, and potentially decreasing recall rates and costs. The inferred 3-dimensional geometry of the breast lesions based on the analysis of the mammographic images using the 2D WTMM methodology allows us to explore the invasiveness of the breast tumors and provide an interpretation of the severity of the lesion. By considering where each case falls on the CC-MLO fractal dimension plot, a score similar to the BIRADs assessment score [14] may be assigned to each case. Not only does this tool have the potential as a CAD, but it may also provide insight into the underlying mechanisms that drive the overall growth and structure at the time of the screening mammogram. In this context, further analyses will help prove or disprove our conjecture that all MC clusters are restricted to growth on 2D manifolds within the 3D environment of the breast tissue.

Since the structure of the tumors are different, with benign lesions likely being smooth Euclidean objects and malignant lesions being branching objects (and possibly, for both cases, being restricted to growing along 2D manifolds within the 3D breast tissue environment), there may be a link to the cellular mechanisms at the lower levels in the system that drive the organization at the much larger scale of mammograms. There has been research done on the shape of cells and also the vascular structure feeding tumors [17,73]. Studies such as these have shown the fractal structure of cancer at these levels, implying the global shape of the breast tumors may be driven by the interactions of smaller scale agents and their environment.

The nature of this study is exploratory. Future analyses on larger sets will allow the investigation of the automation of the selection process for the thresholds on h and on $\log(K)$. The delineation of the boundary between the fractal zone and the Euclidean zones in the CC-MLO fractal dimension plot, which was defined somewhat qualitatively, should also be explored. However, even though the size of the dataset investigated in this study is indeed limited, the robust statistical conclusions that are drawn from the analysis did take into account this limited sample size. Finally, the mathematical and computational approaches, as well as the results presented herein are novel and show great promise towards the establishment of a new paradigm in mammographic breast lesion detection and assessment.

Methods

Data

The images that were analyzed were obtained from the Digital Database for Screening Mammography (DDSM) at the University of South Florida [74,75]. The databank contains over 2,600 studies made up of normal, benign, benign without call back and malignant mammograms all categorized by an expert radiologist. Each study has two images of each breast, consisting of a mediolateral-oblique (MLO) view and cranio-caudal (CC) view with any suspicious region circled by a radiologist. The suspicious region could contain a mass and/or microcalcifications (MC), but only the cases that were classified as having exactly one tumor composed of only microcalcifications in the benign and malignant categories were looked at in this particular study.

In addition to only considering tumors consisting of MC, any mammographic images that contained artifacts inside the radiologist's encircled region were discarded due to the impact it has on the analysis. These artifacts could include scratches, hair, deodorant, patient movement, scanner artifacts (rollers slipped), pacemaker, breast implants, skin markers (for scars, moles, and nipples, as well as marked lumps of breast pain), metallic foreign

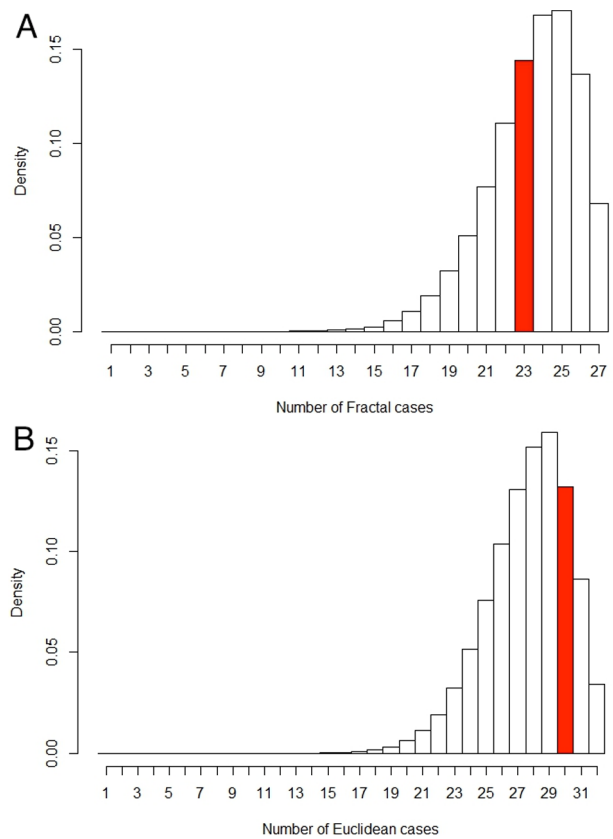


Figure 7. Density histograms of malignant/benign cases out of fractal/Euclidean cases. (A) Histogram of potential malignant cases out of 27 fractal cases given the posterior distribution $p(M|F)$ (see Methods section). The red bar represents our testing data set of 23 malignant cases out of 27 total fractal cases. The probability of arriving at less than or equal to 23 cases is $\sim 46\%$. (B) Histogram of potential benign cases out of 32 Euclidean cases given the posterior distribution $p(B|E)$. The red bar represents our testing data set of 30 benign cases out of a total of 32 Euclidean cases. The probability of arriving at less than or equal to 30 cases is $\sim 74\%$. Since 23 malignant cases (A) and 30 benign cases (B) are not towards either end of these distributions resulting from 100,000 “coin-toss” iterations, we can safely say that the respective models are an adequate fit for the data.
doi:10.1371/journal.pone.0107580.g007

bodies, and fingerprints. Some (but not all) of these effects were recorded under notes in the DDSM website. More information on the extra care required to make efficient use of the DDSM as well as a general discussion on the next-generation open-access digital mammography library can be found in [76]. We thus considered a total of 59 cases corresponding to 118 images of size greater than 256^2 pixels, 34 of which are benign (68 images) and 25 of which are malignant (50 images).

2D WTMM Method

Most of the existing CAD methods, whether specifically designed for (2D) mammograms [32,33,77–91] or more recently, for (3D) breast tomosynthesis [92–97], have been elaborated on the prerequisite that the background roughness fluctuations of normal breast texture are statistically homogeneous and uncorrelated, which precludes their ability to adequately characterize background tissue. The majority of the fractal methods used to examine and classify mammographic breast lesions rely on the estimate of the Hurst exponent (or its various mathematical

equivalents), which globally characterizes the self-similar properties of the landscape in question. However, the 2D WTMM method takes in account that the function defining the image may be multifractal, therefore requiring the use of the Hölder exponent (Eq. (1)) to characterize the local regularity at a particular point [39,40,55,56,63].

The 2D WTMM method [39] requires us to define a smoothing function $\mathcal{G}(x,y)$ in two dimensions that is a well-localized isotropic function around the origin. In this application, we use the Gaussian function and define the wavelets as [64]

$$\psi_1(x,y) = \frac{\partial \mathcal{G}(x,y)}{\partial x} \text{ and } \psi_2(x,y) = \frac{\partial \mathcal{G}(x,y)}{\partial y} \quad (2)$$

The wavelet transform with respect to ψ_1 and ψ_2 is

$$\mathbf{T}_\psi[f](\mathbf{b},a) = \begin{pmatrix} T_{\psi_1}[f] = a^{-2} \int d^2\mathbf{x} \psi_1(a^{-1}(\mathbf{x}-\mathbf{b}))f(\mathbf{x}) \\ T_{\psi_2}[f] = a^{-2} \int d^2\mathbf{x} \psi_2(a^{-1}(\mathbf{x}-\mathbf{b}))f(\mathbf{x}) \end{pmatrix} \quad (3)$$

$$= \mathbf{T}_\psi[f](\mathbf{b},a) = \nabla\{\mathbf{T}\mathcal{G}[f](\mathbf{b},a)\} \quad (4)$$

from which we can extract the modulus and argument of the WT:

$$\mathbf{T}_\psi[f](\mathbf{b},a) = (\mathcal{M}_\psi[f](\mathbf{b},a), \mathcal{A}_\psi[f](\mathbf{b},a)). \quad (5)$$

where

$$\mathcal{M}_\psi[f](\mathbf{b},a) = [(T_{\psi_1}[f](\mathbf{b},a))^2 + T_{\psi_2}[f](\mathbf{b},a)^2]^{\frac{1}{2}} \quad (6)$$

$$\mathcal{A}_\psi[f](\mathbf{b},a) = \text{Arg}\left(T_{\psi_1}[f](\mathbf{b},a) + iT_{\psi_2}[f](\mathbf{b},a)\right) \quad (7)$$

The wavelet transform modulus maxima are defined as the locations \mathbf{b} where $\mathcal{M}_\psi[f](\mathbf{b},a)$ is locally maximum in the direction of the argument $\mathcal{A}_\psi[f](\mathbf{b},a)$ at a given scale $a > 0$. The WTMM lie on connected chains and are thus called maxima chains (Fig. 1) [39,40,55,56]. Additional algorithmic details can be found in the Appendix of reference [43]. One can then find the maxima along these WTMM chains. The WTMM maxima, or WTMMM are defined as the points along the maxima chains where the $\mathcal{M}_\psi[f](\mathbf{b},a)$ is locally maximum. The WTMMM are linked through scales to form the space-scale skeleton (Fig. 1G). 1G) point to in the limit $a \rightarrow 0^+$. Along these space-scale vertical lines the WTMMM behave as a power-law $\sim a^{h(\mathbf{x})}$ (Eq. (1)) from which one can extract the local Hölder exponent $h(\mathbf{x})$. The multifractal formalism amounts to characterize the relative contributions of each Hölder exponent value via the estimate of the so-called $D(h)$ singularity spectrum defined as the fractal dimension of the set of points \mathbf{x} where $h(\mathbf{x}) = h$. To compute $D(h)$ we therefore use wavelets to partition the surface by defining the partition function directly from the WTMMM in the skeleton [39]:

$$\mathcal{Z}(q,a) = \sum_{\mathcal{L} \in \mathcal{L}(a)} \left(\sup_{(\mathbf{x},a') \in \mathcal{L}, a' \leq a} \mathcal{M}_\psi[f](\mathbf{x},a') \right)^q \quad (8)$$

where $\mathcal{L}(a)$ is the set of all vertical space-scale lines in the skeleton that exist at the given scale $a > 0$ and which contain maxima at any scale $a' \leq a$ and $q \in \mathbb{R}$. One can then define the exponent $\tau(q)$ from the power-law behavior of the partition function:

$$\mathcal{Z}(q,a) \sim a^{\tau(q)}, a \rightarrow 0^+ \quad (9)$$

and the $D(h)$ singularity spectrum of f can be determined from the Legendre transform of the partition function scaling exponent [39]

$$D(h) = \min_q(qh - \tau(q)) \quad (10)$$

In practice, to avoid instabilities in the estimation of the singularity spectrum $D(h)$ through the Legendre transform [98,99], we use h and $D(h)$ as mean quantities defined in a canonical ensemble, i.e. with respect to their Boltzmann weights computed from the WTMMM :

$$W_\psi[f](q, \mathcal{L}, a) = \frac{|\sup_{(\mathbf{x},a') \in \mathcal{L}, a' \leq a} \mathcal{M}_\psi[f](\mathbf{x},a')|^q}{\mathcal{Z}(q,a)} \quad (11)$$

Then one computes the expectation values:

$$h(q,a) = \sum_{\mathcal{L} \in \mathcal{L}(a)} \ln \left| \sup_{(\mathbf{x},a') \in \mathcal{L}, a' \leq a} \mathcal{M}_\psi[f](\mathbf{x},a') \right| W_\psi[f](q, \mathcal{L}, a) \quad (12)$$

and

$$D(q,a) = \sum_{\mathcal{L} \in \mathcal{L}(a)} W_\psi[f](q, \mathcal{L}, a) \ln(W_\psi[f](q, \mathcal{L}, a)) \quad (13)$$

from which one derives

$$h(q) = \frac{d\tau(q)}{dq} = \lim_{a \rightarrow 0^+} h(q,a) / \ln a \quad (14)$$

$$D(q) = \lim_{a \rightarrow 0^+} D(q,a) / \ln a \quad (15)$$

and thus the singularity spectrum $D(h)$ as a curve parameterized by q .

Homogeneous monofractal functions with singularities of unique Hölder exponent H are characterized by a linear $\tau(q)$ curve of slope H . A nonlinear $\tau(q)$ is the signature of nonhomogeneous multifractal functions, meaning that the Hölder exponent is a fluctuating quantity [39,98,99] that depends on \mathbf{x} . Then the corresponding singularity spectrum has a characteristic single-humped shape. Note that for both mono- and multifractal functions

$$D(q=0) = -\tau(q=0) = D_F \quad (16)$$

where D_F (noted simply D throughout the text) is the fractal dimension of the support of singularities of f .

Statistical Tests

The Wilcoxon rank-sum test is a non-parametric statistical hypothesis test that is used as an alternative to Student's t -test

when the population cannot be assumed to be normally distributed. It was used here to calculate the p -values comparing the CC and MLO fractal dimensions and benign and malignant cases images since the benign data followed a bimodal distribution (Fig. 4). The calculations were done using the Wilcox test in R.

Bayesian Statistics

Bayes theorem states that

$$p(\theta|G) = \frac{p(G|\theta) \cdot p(\theta)}{p(G)} \quad (17)$$

*posterior = likelihood * prior / evidence*

where the prior, $p(\theta)$, represents the strength of our belief in malignant lesions ($p(M)$) or benign lesions ($p(B)$) out of those that have been diagnosed by a radiologist. The posterior, $p(\theta|G)$, represents the strength of our belief, having accounted for the geometrical evidence, G , where G represents the position of the lesion in the fractal dimension plot, either fractal (F) or Euclidean (E). The quotient of the likelihood over the evidence, $p(G|\theta)/p(G)$, represents the support the evidence, G , provides for θ . Since the prior reflects uncertainty in the parameter value θ , $p(\theta)$ was based on a Beta distribution with a specified mean and standard deviation. The Beta distribution is as follows:

$$f(\theta; \alpha, \beta) = \frac{\Gamma(\alpha + \beta)}{\Gamma(\alpha)\Gamma(\beta)} \theta^{\alpha-1} (1-\theta)^{\beta-1} \quad (18)$$

The Probability Model. To estimate the mean of the Beta distribution for malignant cases, $p(M)$, the prevalence of mammograms with a BI-RADS assessment score of 3, 4, and 5 were used as determined by the radiologists diagnostics multiplied by the historical probability of mammograms receiving those assessment scores result in malignant MC clusters respectively. One out of the 59 cases considered in this study received an assessment score of 3, 47 out of 59 received a 4, and 11 out of 59 received a 5. Based on historical data [14,66,67], the probability of malignant lesions given an assessment score of 3 is 2%, an assessment score of 4 is 26.5% (taken as the midpoint of the reported interval of [23%–30%]), and an assessment score of 5 is 95%. Therefore the Beta distribution for $p(M)$ was chosen with a mean of

$$\frac{1 * 0.02 + 47 * 0.265 + 11 * 0.95}{1 + 47 + 11} = 0.3885$$

and the Beta distribution for $p(B)$ with a mean of $1 - 0.3885 = 0.6115$. However, since there isn't much certainty regarding these values, the Beta distribution for $p(M)$ and $p(B)$ were assigned a relatively large standard deviation of 0.25. This

References

- Onega T, Anderson ML, Miglioretti DL, Buist DS, Geller B, et al. (2013) Establishing a gold standard for test sets: variation in interpretive agreement of expert mammographers. *Acad Radiol* 20: 731–739.
- Jorgensen KJ, Gotzsche PC (2009) Overdiagnosis in publicly organised mammography screening programmes: systematic review of incidence trends. *BMJ* 339: b2587.
- Autier P, Boniol M, Middleton R, Dore JF, Hery C, et al. (2011) Advanced breast cancer incidence following population-based mammographic screening. *Ann Oncol* 22: 1726–1735.
- Jorgensen KJ (2012) Is the tide turning against breast screening? *Breast Cancer Res* 14: 107.
- Jorgensen KJ, Brodersen J, Gotzsche PC (2013) Thirteen years of breast screening had no measurable effect on breast cancer mortality in Norway. *Int J Cancer* 132: 1725–1726.
- Fenton JJ, Xing G, Elmore JG, Bang H, Chen SL, et al. (2013) Short-term outcomes of screening mammography using computer-aided detection: a population-based study of medicare enrollees. *Ann Intern Med* 158: 580–587.
- Fenton JJ, Taplin SH, Carney PA, Abraham L, Sickles EA, et al. (2007) Influence of computer-aided detection on performance of screening mammography. *N Engl J Med* 356: 1399–1409.
- Fenton JJ, Abraham L, Taplin SH, Geller BM, Carney PA, et al. (2011) Effectiveness of computer-aided detection in community mammography practice. *J Natl Cancer Inst* 103: 1152–1161.
- Noble M, Bruening W, Uhl S, Schoelles K (2009) Computer-aided detection mammography for breast cancer screening: systematic review and meta-analysis. *Arch Gynecol Obstet* 279: 881–890.
- Eadie LH, Taylor P, Gibson AP (2012) A systematic review of computer-assisted diagnosis in diagnostic cancer imaging. *Eur J Radiol* 81: e70–76.

resulted in a Beta distribution for $p(M)$ with parameters $(\alpha, \beta) = (1.09241, 1.71223)$ and $p(B)$ with parameters $(\alpha, \beta) = (1.71223, 1.09241)$. The likelihood $p(F|M)$, where F represents breast lesions characterized as being in the fractal zone (and E likewise represents those in the Euclidean zone), is based on the 23 of the 25 malignant cases that were in the fractal zone; this likelihood is the probability that the data could be generated with parameter values θ . Similarly, the likelihood $p(E|B)$ is based on the 30 out of 34 benign cases that were in the Euclidean zone. To arrive at the posterior distributions $p(M|F)$ and $p(B|E)$, the R routine “BernBeta.R” was used, as defined in [65].

The resulting posterior distribution for $p(M|F)$ was a Beta distribution with parameters $(\alpha = 24.0924, \beta = 3.71223)$. Based on this distribution, the resulting 95% highest density interval was (0.742, 0.975). The posterior distribution for $p(B|E)$ was a Beta distribution with parameters $(\alpha = 32.7122, \beta = 5.09241)$. Based on this distribution, the resulting 95% highest density interval was (0.757, 0.962). The highest density interval spans 95% of the posterior distribution such that every point inside the interval is deemed more credible. In other words, given the prior and the likelihood, observing the parameter value for the percentage of breast lesions characterized in the fractal zone that are malignant, there is a 95% probability that this parameter is between 0.742 and 0.975. Similarly, for the percentage of breast lesions characterized in the Euclidean zone that are benign, there is a 95% probability that this parameter is between 0.757 and 0.962.

Statistical “coin toss” experiment

A random sample was taken from the posterior distribution, which gives a sample probability of a malignant case given fractal characterization, and similarly a benign case given Euclidean characterization. This probability was used to conduct the “coin toss” 27 times, which is the total number of cases in the fractal zone (23 malignant and 4 benign) and 32 times, which is the total number of cases in the Euclidean zones (30 benign and 2 malignant), all based on the posterior distribution. This random sampling was performed 100,000 times to arrive at a discrete probability distribution, i.e. a histogram, as shown in Fig. 7.

Acknowledgments

We thank Dr. Amy Harrow, MD, for help and fruitful discussions.

Author Contributions

Conceived and designed the experiments: AK AA KB. Performed the experiments: KB AT LG AK. Analyzed the data: KB AT SA LG PK AA AK. Contributed reagents/materials/analysis tools: AT PK AK. Wrote the paper: KA AA AK.

11. Kim SJ, Moon WK, Seong MH, Cho N, Chang JM (2009) Computer-aided detection in digital mammography: false-positive marks and their reproducibility in negative mammograms. *Acta Radiol* 50: 999–1004.
12. Gilbert FJ, Astley SM, Gillan MG, Agbaje OF, Wallis MG, et al. (2008) Single reading with computer-aided detection for screening mammography. *N Engl J Med* 359: 1675–1684.
13. Georgian-Smith D, Moore RH, Halpern E, Yeh ED, Rafferty EA, et al. (2007) Blinded comparison of computer-aided detection with human second reading in screening mammography. *AJR Am J Roentgenol* 189: 1135–1141.
14. Eberl MM, Fox CH, Edge SB, Carter CA, Mahoney MC (2006) BI-RADS classification for management of abnormal mammograms. *J Am Board Fam Med* 19: 161–164.
15. England PH (2013) NHS Breast Cancer Screening Programme: Age Extension Full Randomised Control Trial.
16. Mandelbrot BB (1983) *The fractal geometry of nature*. New York: W.H. Freeman. 468 p., C416 p. of plates p.
17. Bizzarri M, Giuliani A, Cucina A, D'Anselmi F, Soto AM, et al. (2011) Fractal analysis in a systems biology approach to cancer. *Semin Cancer Biol* 21: 175–182.
18. Baish JW, Jain RK (2000) Fractals and cancer. *Cancer Res* 60: 3683–3688.
19. Cross SS (1997) Fractals in pathology. *J Pathol* 182: 1–8.
20. Losa GM, D; Nonnenmacher, TF; Weibel, ER (2002) *Fractals in Biology and Medicine*. Basel: Birkhauser Verlag.
21. Bunk W, Jamitzky F, Pompl R, Rath C, Morfill G (2002) Local scaling properties for diagnostic purposes. In: Bunde A, Kropp J, Schelinhuber H, editors. *The Science of Disasters*. 282–309.
22. Cross SS, McDonagh AJ, Stephenson TJ, Cotton DW, Underwood JC (1995) Fractal and integer-dimensional geometric analysis of pigmented skin lesions. *Am J Dermatopathol* 17: 374–378.
23. Claridge E, Hall PN, Keefe M, Allen JP (1992) Shape analysis for classification of malignant melanoma. *J Biomed Eng* 14: 229–234.
24. Gazit Y, Berk DA, Leunig M, Baxter LT, Jain RK (1995) Scale-invariant behavior and vascular network formation in normal and tumor tissue. *Phys Rev Lett* 75: 2428–2431.
25. Michaelson JS, Cheongiatmoy JA, Dewey F, Silverstein MJ, Sgroi D, et al. (2005) Spread of human cancer cells occurs with probabilities indicative of a nongenetic mechanism. *Br J Cancer* 93: 1244–1249.
26. Tracqui P (2009) Biophysical model of tumor growth. *Rep Prog Phys* 72: 1–30.
27. Landini G, Rippin J (1996) How important is tumor shape? Quantification of the epithelial connective tissue interface in oral lesions using local connected fractal dimension analysis. *J Pathol* 179: 210–217.
28. Eid R, Landini G (2003) Quantification of the global and local complexity of the epithelial-connective tissue interface of normal, dysplastic, and neoplastic oral mucose using digital imaging. *Pathol Res Pract* 199: 475–482.
29. Lefebvre F, Benali H, Gilles R, Kahn E, Di Paola R (1995) A fractal approach to the segmentation of microcalcifications in digital mammograms. *Med Phys* 22: 381–390.
30. Li H, Liu KJ, Lo SC (1997) Fractal modeling and segmentation for the enhancement of microcalcifications in digital mammograms. *IEEE Trans Med Imaging* 16: 785–798.
31. Sankar D, Thomas T (2010) A new fast fractal modeling approach for the detection of microcalcifications in mammograms. *J Digit Imaging* 23: 538–546.
32. Rangayyan RM, Nguyen TM (2007) Fractal analysis of contours of breast masses in mammograms. *J Digit Imaging* 20: 223–237.
33. Raguso G, Ancona A, Chieppa L, L'Abbate S, Pepe ML, et al. (2010) Application of fractal analysis to mammography. *Conf Proc IEEE Eng Med Biol Soc* 2010: 3182–3185.
34. Rangayyan RM, Oloumi F, Nguyen TM (2010) Fractal analysis of contours of breast masses in mammograms via the power spectra of their signatures. *Conf Proc IEEE Eng Med Biol Soc* 2010: 6737–6740.
35. Yamada K, Yabashi S, Hata M. Quantitative expression of microcalcification distribution in mammograph by using fractal dimension; 1992 16–20 Nov 1992. 92–96 vol.91.
36. Bocchi L, Coppini G, Nori J, Valli G (2004) Detection of single and clustered microcalcifications in mammograms using fractals models and neural networks. *Med Eng Phys* 26: 303–312.
37. Stotzka R, Mueller TO, Epper W, Gemmeke H Three-dimensional reconstruction of clustered microcalcifications from two digitized mammograms. *Medical Imaging 1998: Image Processing* 3338: 513–520.
38. Ma L, Shan Y (2008) Detections of microcalcification clusters using multiple mammographic views. *The 2nd International Conference on Bioinformatics and Biomedical Engineering*: 361–365.
39. Arneodo A, N Decoster, P Kestener, S.G Roux (2003) A wavelet-based method for multifractal image analysis: From theoretical concepts to experimental applications. *Adv Imaging Electr Phys* 126: 1–92.
40. Roux S, Decoster N, Arneodo A (2000) A wavelet-based method for multifractal image analysis. III. Applications to high-resolution satellite images of cloud structure. *Eur Phys J B* 15: 765–786.
41. Khalil A, Jonas G, Nekka F, Kestener P, Arneodo A (2006) Morphological analysis of HI features. II. Wavelet-based multifractal formalism. *Astrophys J Suppl S* 165: 512–550.
42. Kestener P, Conlon PA, Khalil A, Fennell L, McAteer R, et al. (2010) Characterizing complexity in Solar magnetogram data using a wavelet-based segmentation method. *Astrophys J* 717: 995–1005.
43. McAteer RJ, Kestener P, Arneodo A, Khalil A (2010) Automated detection of coronal loops using a wavelet transform modulus maxima method. *Sol Phys* 262: 387–397.
44. Roland T, Khalil A, Tanenbaum A, Berguiga L, Delichère P, et al. (2009) Revisiting the physical processes of vapodeposited thin gold films on chemically modified glass by atomic force and surface plasmon microscopies. *Surf Sci* 603: 3307–3320.
45. Caddle LB, Grant JL, Szatkiewicz J, van Hase J, Shirley BJ, et al. (2007) Chromosome neighborhood composition determines translocation outcomes after exposure to high-dose radiation in primary cells. *Chromosome Res* 15: 1061–1073.
46. Khalil A, Grant JL, Caddle LB, Atzema E, Mills KD, et al. (2007) Chromosome territories have a highly nonspherical morphology and nonrandom positioning. *Chromosome Res* 15: 899–916.
47. Snow CJ, Peterson MT, Khalil A, Henry CA (2008) Muscle development is disrupted in zebrafish embryos deficient for fibronectin. *Dev Dyn* 237: 2542–2553.
48. Snow CJ, Goody M, Kelly MW, Oster EC, Jones R, et al. (2008) Time-lapse analysis and mathematical characterization elucidate novel mechanisms underlying muscle morphogenesis. *PLoS Genet* 4: e1000219.
49. Goody MF, Kelly MW, Lessard KN, Khalil A, Henry CA (2010) Nrk2b-mediated NAD⁺ production regulates cell adhesion and is required for muscle morphogenesis in vivo: Nrk2b and NAD⁺ in muscle morphogenesis. *Dev Biol* 344: 809–826.
50. Grant J, Verrill C, Coustham V, Arneodo A, Palladino F, et al. (2010) Perinuclear distribution of heterochromatin in developing *C. elegans* embryos. *Chromosome Res* 18: 873–885.
51. Goody MF, Kelly MW, Reynolds CJ, Khalil A, Crawford BD, et al. (2012) NAD⁺ biosynthesis ameliorates a zebrafish model of muscular dystrophy. *PLoS Biol* 10: e1001409.
52. Khalil A, Aponte C, Zhang R, Davisson T, Dickey I, et al. (2009) Image analysis of soft-tissue in-growth and attachment into highly porous alumina ceramic foam metals. *Med Eng Phys* 31: 775–783.
53. Muzy JF, Bacry E, Arneodo A (1991) Wavelets and multifractal formalism for singular signals: Application to turbulence data. *Phys Rev Lett* 67: 3515–3518.
54. Muzy JF, Bacry E, Arneodo A (1993) Multifractal formalism for fractal signals: The structure-function approach versus the wavelet-transform modulus-maxima method. *Phys Rev E Stat Phys Plasmas Fluids Relat Interdiscip Topics* 47: 875–884.
55. Arneodo A, Decoster N, Roux S (2000) A wavelet-based method for multifractal image analysis. I. Methodology and test applications on isotropic and anisotropic random rough surfaces. *Eur Phys J B* 15: 567–600.
56. Decoster N, Arneodo A, Roux S (2000) A wavelet-based method for multifractal image analysis. II. Applications to synthetic multifractal rough surfaces. *Eur Phys J B* 15: 739–764.
57. Kestener P, Arneodo A (2003) Three-dimensional wavelet-based multifractal method: The need for revisiting the multifractal description of turbulence dissipation data. *Phys Rev Lett* 91: 194501.
58. Ivanov PC, Amaral LA, Goldberger AL, Havlin S, Rosenblum MG, et al. (1999) Multifractality in human heartbeat dynamics. *Nature* 399: 461–465.
59. Ivanov PC, Nunes Amaral LA, Goldberger AL, Havlin S, Rosenblum MG, et al. (2001) From 1/f noise to multifractal cascades in heartbeat dynamics. *Chaos* 11: 641–652.
60. Nunes Amaral LA, Ivanov PC, Aoyagi N, Hidaka I, Tomono S, et al. (2001) Behavioral-independent features of complex heartbeat dynamics. *Phys Rev Lett* 86: 6026–6029.
61. Gerasimova E, Audit B, Roux SG, Khalil A, Argoul F, et al. (2013) Multifractal analysis of dynamic infrared imaging of breast cancer. *EPL* 104:68001.
62. Gerasimova E, Audit B, Roux SG, Khalil A, Gileva O, et al. (2014) Wavelet-based multifractal analysis of dynamic infrared thermograms to assist in early breast cancer diagnosis. *Front Phys doi:10.3389/fphys.2014.00176*.
63. Kestener P, Lina J.M., St-Jean P., Arneodo A. (2001) Wavelet-based multifractal formalism to assist in diagnosis in digitized mammograms. *Image Anal Stereol* 20: 169–174.
64. Mallat S (1998) *A Wavelet Tour of Signal Processing*: Academic Press: New York.
65. Kruschke JK (2011) *Doing Bayesian data analysis a tutorial with R and BUGS*. Burlington, Mass.: Academic Press.
66. Lacquement MA, Mitchell D, Hollingsworth AB (1999) Positive predictive value of the Breast Imaging Reporting and Data System. *J Am Coll Surg* 189: 34–40.
67. Orel SG, Kay N, Reynolds C, Sullivan DC (1999) BI-RADS categorization as a predictor of malignancy. *Radiology* 211: 845–850.
68. Gelman A, Carlin J, Stern H, Dunson D, Vehtari A, et al. (2013) *Bayesian Data Analysis, Third Edition*: Chapman & Hall/CRC Texts in Statistical Science.
69. Witten Jr T, Sander LM (1981) Diffusion-limited aggregation, a kinetic critical phenomenon. *Phys Rev Lett* 47: 1400–1403.
70. Hunt BR, Kaloshin VY (1997) How projections affect the dimension spectrum of fractal measures. *Nonlinearity* 10: 1031–1046.
71. Argoul F, A Arneodo, G Grasseau, HL Swinney (1988) Self-similarity of diffusion-limited aggregates and electrodeposition clusters. *Phys Rev Lett* 61: 2558–2561.
72. Khun A, Argoul F, JF Muzy, A Arneodo (1994) Structural analysis of electrodeless deposits in the diffusion-limited regime. *Phys Rev Lett* 73: 2998–3001.

73. D'Anselmi F, Valerio M, Cucina A, Galli L, Proietti S, et al. (2011) Metabolism and cell shape in cancer: a fractal analysis. *Int J Biochem Cell Biol* 43: 1052–1058.
74. Heath M, K Bowyer, D Kopans, W P Kegelmeyer, R Moore, K Chang, S. MunishKumaran. Current status of the Digital Database for Screening Mammography. *Digital Mammography*; 1998. pp. 457–460.
75. Heath M, K Bowyer, D Kopans, R Moore, W P Kegelmeyer. The Digital Database for Screening Mammography. In: Yaffe MJ, editor; 2001. pp. 212–218.
76. Horsch A, Hapfelmeier A, Elter M (2011) Needs assessment for next generation computer-aided mammography reference image databases and evaluation studies. *Int J Comput Assist Radiol Surg* 6: 749–767.
77. Karahaliou AN, Boniatis IS, Skiadopoulos SG, Sakellaropoulos FN, Arikidis NS, et al. (2008) Breast cancer diagnosis: analyzing texture of tissue surrounding microcalcifications. *IEEE Trans Inf Technol Biomed* 12: 731–738.
78. Zanca F, Jacobs J, Van Ongeval C, Claus F, Celis V, et al. (2009) Evaluation of clinical image processing algorithms used in digital mammography. *Med Phys* 36: 765–775.
79. Ke L, He W, Kang Y (2009) Mass auto-detection in mammogram based on wavelet transform modulus maximum. *Conf Proc IEEE Eng Med Biol Soc*: 5760–5763.
80. Manduca A, Carston MJ, Heine JJ, Scott CG, Pankratz VS, et al. (2009) Texture features from mammographic images and risk of breast cancer. *Cancer Epidemiol Biomarkers Prev* 18: 837–845.
81. Ayer T, Ayvaci MU, Liu ZX, Alagoz O, Burnside ES (2010) Computer-aided diagnostic models in breast cancer screening. *Imaging Med* 2: 313–323.
82. Meselhy Eltoukhy M, Faye I, Belhaouari Samir B (2010) A comparison of wavelet and curvelet for breast cancer diagnosis in digital mammogram. *Comput Biol Med* 40: 384–391.
83. Kilic N, Gorgel P, Ucan ON, Sertbas A (2010) Mammographic mass detection using wavelets as input to neural networks. *J Med Syst* 34: 1083–1088.
84. Tsai NC, Chen HW, Hsu SL (2011) Computer-aided diagnosis for early-stage breast cancer by using Wavelet Transform. *Comput Med Imaging Graph* 35: 1–8.
85. Alzubi S, Islam N, Abbod M (2011) Multiresolution analysis using wavelet, ridgelet, and curvelet transforms for medical image segmentation. *Int J Biomed Imaging*: 136034.
86. Reiser I, Lee S, Nishikawa RM (2011) On the orientation of mammographic structure. *Med Phys* 38: 5303–5306.
87. Issac Niwas S, Palanisamy P, Chibbar R, Zhang WJ (2012) An expert support system for breast cancer diagnosis using color wavelet features. *J Med Syst* 36: 3091–3102.
88. Meselhy Eltoukhy M, Faye I, Belhaouari Samir B (2012) A statistical based feature extraction method for breast cancer diagnosis in digital mammogram using multiresolution representation. *Comput Biol Med* 42: 123–128.
89. Thangavel K, Velayutham C (2012) Unsupervised feature selection in digital mammogram image using rough set theory. *Int J Bioinform Res Appl* 8: 436–454.
90. Velayutham C, Thangavel K (2012) Entropy based unsupervised feature selection in digital mammogram image using rough set theory. *Int J Comput Biol Drug Des* 5: 16–34.
91. Haberle L, Wagner F, Fasching PA, Jud SM, Heusinger K, et al. (2012) Characterizing mammographic images by using generic texture features. *Breast Cancer Res* 14: R59.
92. Reiser I, Nishikawa RM, Giger ML, Wu T, Rafferty E, et al. (2004) Computerized detection of mass lesions in digital breast tomosynthesis images using two- and three dimensional radial gradient index segmentation. *Technol Cancer Res Treat* 3: 437–441.
93. Chan HP, Wei J, Sahiner B, Rafferty EA, Wu T, et al. (2005) Computer-aided detection system for breast masses on digital tomosynthesis mammograms: preliminary experience. *Radiology* 237: 1075–1080.
94. Reiser I, Nishikawa RM, Giger ML, Wu T, Rafferty EA, et al. (2006) Computerized mass detection for digital breast tomosynthesis directly from the projection images. *Med Phys* 33: 482–491.
95. Chan HP, Wei J, Zhang Y, Helvie MA, Moore RH, et al. (2008) Computer-aided detection of masses in digital tomosynthesis mammography: comparison of three approaches. *Med Phys* 35: 4087–4095.
96. Singh S, Tourassi GD, Baker JA, Samei E, Lo JY (2008) Automated breast mass detection in 3D reconstructed tomosynthesis volumes: a featureless approach. *Med Phys* 35: 3626–3636.
97. Reiser I, Nishikawa RM, Edwards AV, Kopans DB, Schmidt RA, et al. (2008) Automated detection of microcalcification clusters for digital breast tomosynthesis using projection data only: a preliminary study. *Med Phys* 35: 1486–1493.
98. Muzy J, E Bacry, A Arneodo (1994) The multifractal formalism revisited with wavelets. *Int J Bifurc Chaos* 4: 245–302.
99. Arneodo A, E Bacry, JF Muzy (1995) The thermodynamics of fractals revisited with wavelets. *Physica A* 213: 232–275.